

Synthesis and photoelectrochemical properties of visible-light response g-C₃N₄@CdS heterojunctions photocatalyst

Jinhuan Ma^a, Zhiqiang Wei^{a,b,*}, Ling Li^a, Long Ma^a, Chao Li^a, Shangpan Huang^a

^aSchool of Science, Lanzhou University of Technology, Lanzhou 730050, China, emails: qianweizuo@163.com (Z. Wei), jhma123654@163.com (J. Ma), 1275649863@qq.com (L. Li), mlong163502@163.com (L. Ma), chaoli3067@163.com (C. Li), 15642245364@163.com (S. Huang)

^bState Key Laboratory of Advanced Processing and Recycling of Non-ferrous Metals, Lanzhou University of Technology, Lanzhou 730050, China

Received 13 January 2021; Accepted 2 June 2021

ABSTRACT

g-C₃N₄@CdS nanocomposites with different mass ratios were successfully fabricated by the precipitation method. Different ratios were investigated for their influence on the microstructure, photoelectrochemical, and photocatalytic properties of the as-prepared samples. The experimental results show that g-C₃N₄@CdS nanocomposites are hexagonal structures with good crystallization, and g-C₃N₄ wraps one-dimensional CdS nanorods. g-C₃N₄@CdS nanocomposites exhibit excellent visible-light absorption. The PL spectra, transient photocurrent response, and EIS measurements of g-C₃N₄@CdS composites indicate that heterojunctions accelerate the separation and migration of photo-generated electron-hole pairs and inhibit the recombination of photo-generated carriers. Under simulated sunlight irradiation, the g-C₃N₄@CdS photocatalyst accelerates the redox reaction and improves photocatalytic efficiency to degrade MO, compared to pure photocatalysts. g-C₃N₄@CdS photocatalysts exhibit good degradation efficiency and excellent recyclability. In addition, [•]O₂ and [•]OH play a key role in the photocatalytic degradation process.

Keywords: g-C₃N₄@CdS; Heterojunctions; Microstructure; Photocatalytic activity; Photoelectrochemical property

1. Introduction

In recent years, with the continuous progress of science and technology and the rapid development of society, environmental pollution has become a serious problem in the world, and water security is an urgent issue that needs to be solved [1,2]. Organic dye wastewater is difficult to degrade under natural conditions due to its biological toxicity, high concentration, high chroma, causing great harm to human survival and ecological balance [3,4]. Various methods have been developed to remove the pollutant, including chemical oxidation, adsorption, flocculation precipitation, biodegradation, ozone oxidation, and photocatalytic degradation [5–7]. Among them, photocatalysis

is a very effective technology method in degrading toxic water pollutants because the photocatalytic degradation process does not require additional additives or apparatus other than light under mild reaction conditions [8]. Furthermore, this process is high efficiency, low cost, and a friendly environment. Graphitic carbon nitride (g-C₃N₄) is one of the most suitable photocatalysts owing to its narrow band gap (2.85 eV), visible-light response, and good thermal and chemical stability [9,10]. Nevertheless, the low-quantum efficiency and fast recombination rate of photo-generated carriers result in pure g-C₃N₄, limiting its industrial application [11–13]. Therefore, many methods have been utilized to enhance photocatalytic activity,

* Corresponding author.

such as metal doping, defect generation, morphological adjustment, noble metal deposition, and heterojunction construction [14–16]. Among them, constructing heterojunction with low-band gap semiconductors is regarded as one of the most promising methods due to it can not only reduce the band gap and enhance visible-light absorption, but also can accelerate the separation and migration efficiency of photo-generated carriers, and inhibit the recombination of electron-hole pairs [17,18]. In the past several years, CdS as a narrow band gap (2.42 eV) II–IV semiconductor has attracted much attention due to good visible-light response, which can be used to modify other semiconductors with a wide band gap to tunable the band gap and improve photocatalytic activity [19–21]. However, as far as we know, few studies on the effects of the composite ratio on the microstructure, photoelectrochemical and photocatalytic properties of $g\text{-C}_3\text{N}_4\text{@CdS}$ heterojunctions. The CdS and $g\text{-C}_3\text{N}_4$ composite successfully, light absorbance may also be extended to the visible region [22]. The RhB degradation in synergistic photocatalysis inhibits the reverse reaction of Cr(VI) reduction and validly supplies the photo-generated electrons by the photosensitization effect, which may be helpful for rationally designing photocatalysts and providing illuminating insights into the photocatalytic mechanism [23].

In this work, $g\text{-C}_3\text{N}_4\text{@CdS}$ heterojunctions with different mass ratios were successfully fabricated using the precipitation method for advanced photoelectrochemical performance and degradation efficiency. And the microstructure, morphology, photoelectrochemical, and photocatalytic properties of the samples were characterized by X-ray diffraction (XRD), scanning electron microscopy (SEM), high-resolution transmission electron microscopy (HRTEM), X-ray photoelectron spectrometer (XPS), photoluminescence spectroscopy (PL), and UV-Vis diffuse reflection spectroscopy (UV-Vis DRS). Electrochemical impedance spectra (EIS) and transient photocurrent response were tested to evaluate the photo-generated charges' recombination and electron transportation performance. The effects of the composite ratio on the photocatalytic performance of the samples were evaluated by the photodegradation of methylene orange (MO) in an aqueous solution under the simulated sunlight and the possible enhanced visible photocatalytic activity mechanism was also proposed.

2. Experimental

2.1. Synthesis of CdS samples

CdS nanomaterials were prepared via hydrothermal method as follows: cadmium and sulfur sources were weighed at 0.0025 mol Cd (CH_3CO_2)₂ and 0.015 mol $\text{CH}_4\text{N}_2\text{S}$, respectively, and then dissolved in 40 mL deionized water and 40 mL ethylenediamine to obtain a mixed solution. The resulting mixture was sonicated for 30 min before being magnetically stirred for another 30 min to make thorough mixing. Subsequently, the obtained suspension was then transferred to a 100 mL Teflon-lined stainless-steel autoclave and heated at 185°C for 12 h under the hydrothermal strip after the autoclaves were naturally cooled to room temperature. The precipitation was washed

with ethanol and deionized water for three times, repeatedly, and finally CdS samples were collected after vacuum drying at 60°C for 12 h.

2.2. Preparation of $g\text{-C}_3\text{N}_4$ samples

$g\text{-C}_3\text{N}_4$ powders were synthesized by the calcination method. Certain amounts of melamine (analytically pure) have been weighed, grind it, and put in a crucible that was heated in a tubular furnace with a temperature rise rate of 10°C/min. And the tubular furnace was further heated at 550°C for 2 h. After the reaction, the sample was naturally cooled to room temperature.

2.3. Preparation of $g\text{-C}_3\text{N}_4\text{@CdS}$ nanocomposites

In a typical synthesis of the $g\text{-C}_3\text{N}_4\text{@CdS}$ nanocomposites, weighed different amounts of $g\text{-C}_3\text{N}_4$ and CdS samples according to the mass ratio (1:1, 2:1, and 3:1) then mixed in 80 mL deionized water. The resulting mixture was ultrasonic treatment for 60 min, then magnetically stirred for 12 h. Subsequently, the obtained mixed solution was transferred into the oven and kept at 60°C for 12 h. Finally, the mixture was calcined at 300°C for 1 h in a tube furnace to obtain $g\text{-C}_3\text{N}_4\text{@CdS}$ nanocomposites. With the above method, a series of $g\text{-C}_3\text{N}_4\text{@CdS}$ composites with different mass ratios (1:1, 2:1, and 3:1) were obtained via a similar method, and the samples were denoted as CNCS-1, CNCS-2, and CNCS-3, respectively.

2.4. Characterization

The crystal phase composition of the products was recorded on a powder X-ray diffractometer (Rigaku, Japan, D/Max-2400) with Cu K α radiation in an angle range of 10°–80°, scanning rate 0.2°/s and step size 0.02°. The morphology of the as-prepared samples was observed by field emission scanning electron microscope (FESEM, Hitachi S4800) and high-resolution transmission electron microscopy (HRTEM, JEM-2010). The surface chemical composition and chemical state of elements were studied by an X-ray photoelectron spectrometer (XPS, PHI-5702). The optical absorption spectra were measured by an ultraviolet-visible (UV-vis) spectrophotometer (PERSEE TU-1901). The photoluminescence spectra (PL) were recorded by a PerkinElmer spectrophotometer (LS-55) with an excitation wavelength of 500 nm.

2.5. Photoelectrochemical measurement

Electrochemical impedance spectra (EIS), Mott-Schottky curves, and transient photocurrent response were recorded by an electrochemical workstation (CS350, Wuhan CorrTest, China) with a conventional three-electrode system. The working electrodes were prepared by dropping $g\text{-C}_3\text{N}_4\text{@CdS}$ samples onto the surface of the Indium Tin Oxide (ITO) conductive glass; the reference electrode is a saturated calomel electrode (SCE) and a platinum plate as the counter electrode. The electrolyte was 0.1 mol L⁻¹ Na₂SO₄ and the 500 W xenon lamp was used as excitation. The photocurrent-time (I-t) curves were tested under 0.5 V bias. EIS Nyquist plots

were performed in the frequency range from 0.01 Hz to 100 kHz with an amplitude of 5 mV. The flat band potential of the photocatalyst was estimated from the Mott-Schottky curves under different frequencies.

2.6 Photocatalytic experiment

The photocatalytic activity of the as-prepared samples was evaluated by the degradation of methyl orange (MO) under visible-light illumination by the VS-GCH-XE-300 photochemical reaction apparatus. In the degradation experiment, 50 mg photocatalyst were dispersed in the 100 mL MO solution (10 mg L^{-1}). Meanwhile, the suspension was ultrasonicated in the dark for 30 min to ensure the adsorption-desorption equilibrium between the photocatalyst and reactant before illumination. Subsequently, the photocatalytic degradation reaction was carried out for 120 min under 500 W xenon lamp irradiation. After each time intervals (30 min), 4 mL of the reaction solution was taken out. The concentration of MO solution was analyzed by the UV-Vis spectrophotometer in a different time period. After the photocatalytic reaction, collect the dispersed photocatalyst and repeat the photocatalytic degradation experiment under the same conditions.

3. Results and discussion

3.1. Structure and morphology analysis

The typical XRD patterns of pure CdS, pure $\text{g-C}_3\text{N}_4$ and $\text{g-C}_3\text{N}_4@\text{CdS}$ nanocomposites with different mass ratios are shown in Fig. 1. It is obvious that pure $\text{g-C}_3\text{N}_4$ displays two characteristic peaks at $2\theta = 12.9^\circ$ and 27.5° , which are associated with the (100) and (002) diffraction planes of $\text{g-C}_3\text{N}_4$, respectively. The former is related to the in-plane structure stacking pattern, and the latter corresponds to the long-distance inter planar stacking of aromatic systems [24]. For pure CdS, the diffraction peaks appear at 2θ , 24.86° , 26.52° , 28.22° , 36.66° , 43.76° , 47.90° , 51.00° , 51.86° , and 52.86° , which exactly assigned to the crystal planes (100), (002), (101), (102), (110), (103), (200), (112), and (201) of the hexagonal structure of CdS with JPCDS (No. 41–1049), respectively. In addition, the diffraction peaks of $\text{g-C}_3\text{N}_4@\text{CdS}$ nanocomposites with different mass ratios are basically consistent with pure CdS; however, with the introduction of $\text{g-C}_3\text{N}_4$, there is not obviously observed

$\text{g-C}_3\text{N}_4$ diffraction peak, which may be attributed to the strong interaction between CdS and $\text{g-C}_3\text{N}_4$, resulting in the predominant (002) diffraction peak of $\text{g-C}_3\text{N}_4$ ($2\theta = 27.5^\circ$) coincides with the peak at 28.22° of CdS. Compared with pure CdS and $\text{g-C}_3\text{N}_4$, no other peaks are observed for $\text{g-C}_3\text{N}_4@\text{CdS}$ composites, indicating that the $\text{g-C}_3\text{N}_4@\text{CdS}$ samples have been successfully synthesized.

The features of the as-synthesized photocatalysts were examined using the SEM and HRTEM. Fig. 2 illustrates the respective SEM images of pure CdS, pure $\text{g-C}_3\text{N}_4$, and $\text{g-C}_3\text{N}_4@\text{CdS}$ samples. From Fig. 2a, it is clear that the shape of pure CdS mainly exhibits a nano-sized rod structure; the average diameter of the nanorod structure is about 100 nm with an average length ranging from 200 to 400 nm, and there are also some slight agglomerations. From Fig. 2b, pure $\text{g-C}_3\text{N}_4$ exhibits significantly aggregated morphologies, composed of small lumpy particles with a diameter of about 100 nm. Fig. 2c shows SEM images of CNCS-2 nanocomposites, which indicate that $\text{g-C}_3\text{N}_4$ blocky particles are uniformly aggregated in the CdS nanorods to form the composite structure. The lattice constants, half-width and other data of pure CdS and $\text{g-C}_3\text{N}_4@\text{CdS}$ compounded with different mass ratios are shown in Table 1.

To further investigate the microstructure information of $\text{g-C}_3\text{N}_4@\text{CdS}$ nanocomposites, HRTEM images of CNCS-2

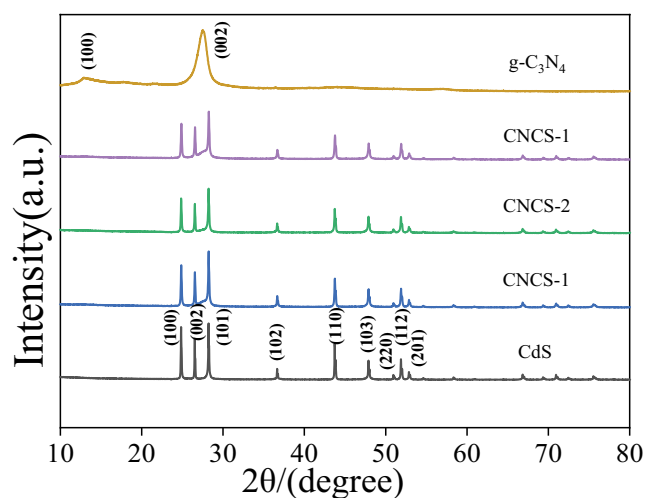


Fig. 1. XRD patterns of CdS, $\text{g-C}_3\text{N}_4$ and $\text{g-C}_3\text{N}_4@\text{CdS}$ samples.

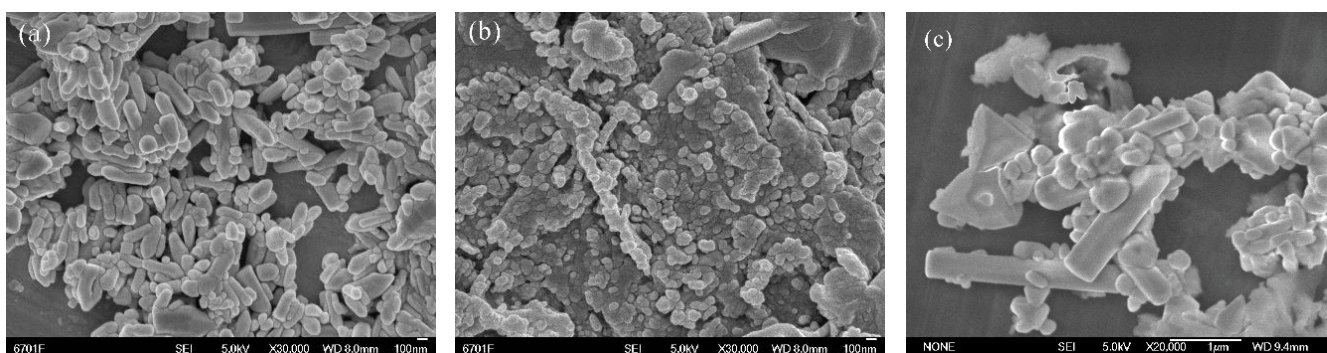


Fig. 2. SEM images of (a) pure CdS, (b) pure $\text{g-C}_3\text{N}_4$ and (c) CNCS-2.

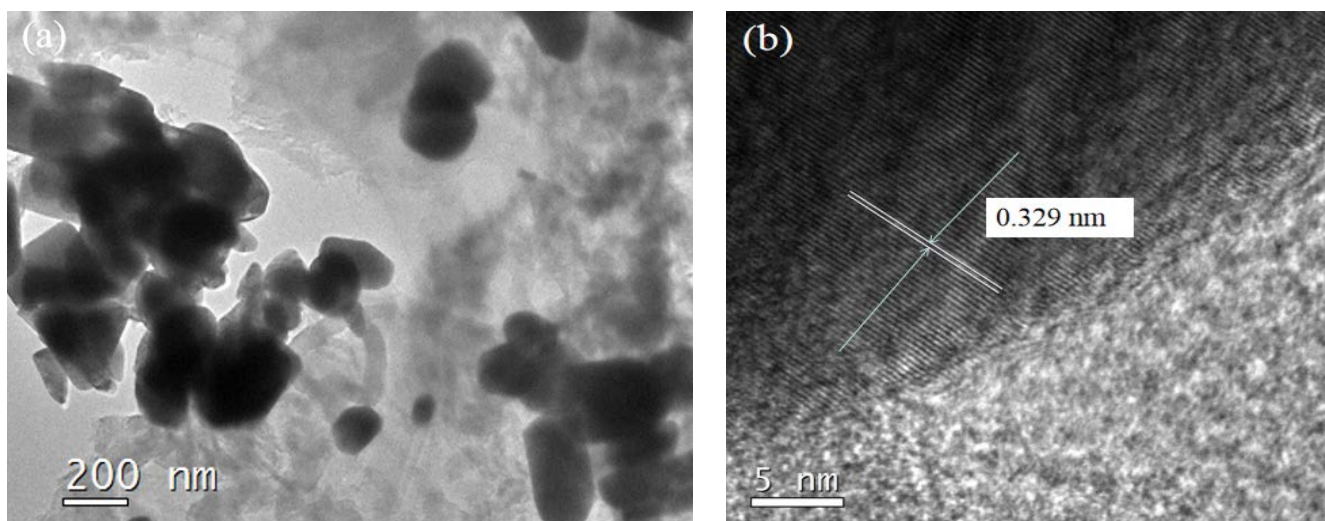


Fig. 3. HRTEM images of CNCS-2.

Table 1
Lattice parameters of pure CdS and g-C₃N₄@CdS samples

Sample	2θ (°)	Grain size (nm)	Unit cell volume (Å ³)	Half width (°)	a (Å)	c (Å)	Interplanar Spacing (Å)	Bond length (nm)	ε (10 ⁻³)	δ (10 ⁻³)
CdS	26.52	51.1	99.3	0.158	4.132	6.716	3.358	0.1093	0.615	41.9
CNCS-1	26.54	72.1	99.2	0.112	4.131	6.711	3.356	0.1092	0.436	52.5
CNCS-2	26.54	69.6	99.3	0.116	4.134	6.712	3.356	0.1092	0.452	51.2
CNCS-3	26.56	71.4	98.9	0.113	4.127	6.706	3.353	0.1090	0.440	52.2

were measured as displayed in Fig. 3. It can be seen that CdS nanorod structures are partially wrapped by g-C₃N₄. The locally amplified HRTEM image of the CNCS-2 sample displays clear lattice fringe as explored in Fig. 3b, the lattice spacing of 0.329 nm corresponding to hexagonal structure CdS (101) crystal planes. This is consistent with the results of CNCS-2 samples obtained by XRD patterns.

To further study the surface chemical composition and electronic element states, high-resolution XPS spectra were performed, as described in Fig. 4a depicts the Cd 3d, S 2p, C 1s, and N 1s XPS spectra of CNCS-2 samples. Fig. 4b displays Cd 3d two characteristic peaks at binding energies of 404.9 and 411.7 eV, corresponding to Cd 3d_{5/2} and Cd 3d_{3/2} states [25,26], respectively, which shows that the Cd element exists in the Cd²⁺ state [27,28]. S 2p can be fitted with S 2p_{3/2} and S 2p_{1/2} as shown in Fig. 4c; two characteristic peaks appear at 161.3 and 162.4 eV, which indicate that the S-element is the S²⁻ state present in the samples [29]. As shown in Fig. 4(d), the C 1s spectrum can be deconvoluted into three peaks with the binding energies of 284.8, 286.4, and 288.3 eV, corresponding to the characteristic peaks C–C, C=C/C≡C, and C–N₃ bonds, respectively. In addition, N 1s spectrum (Fig. 4e) is resolved into three characteristic peaks at 398.6, 399.4, and 401.1 eV, which are assigned to C–N=C, N–(C)₃, and C–N–H bonds, respectively [30,31].

The UV-vis DRS and the corresponding first derivative curves of pure CdS, pure g-C₃N₄, and g-C₃N₄@CdS samples are displayed in Fig. 5. The band gap energy

of the samples related to the electron transition from the VB to the CB can be calculated from the position of the absorption edges. Pure CdS displays the absorption edge at approximately 514 nm (2.42 eV), while pure g-C₃N₄ samples are observed at 434 nm (2.85 eV), which corresponds to the characteristic band edge emission [32,33]. For binary g-C₃N₄@CdS composites display visible-range absorption features, the absorption edges of g-C₃N₄@CdS composites exhibit a slight red shift trend compared with that of pure CdS, the estimated band gap values for g-C₃N₄ > CdS > CNCS-3 > CNCS-1 > CNCS-2, and CNCS-2 exhibit the smallest band gap (2.42 eV). The visible-light absorbance of g-C₃N₄@CdS heterojunction is ascribed to the chemical bonding interaction between CdS and g-C₃N₄, which will allow more photons to be captured, thus forming more carrying and enhancing the photocatalytic reaction [34].

3.2. PL analysis

The PL emission intensity is related to the recombination efficiency of photo-generated electron-hole pairs in the photocatalytic system. In order to prove the effective separation of photo-generated charges, PL spectra of pure g-C₃N₄ and g-C₃N₄@CdS samples were performed to verify the charge transfer mechanism. As shown in Fig. 6, it is obvious that pure g-C₃N₄ exhibits the strongest PL emission signal in the range of 630–700 nm, implying

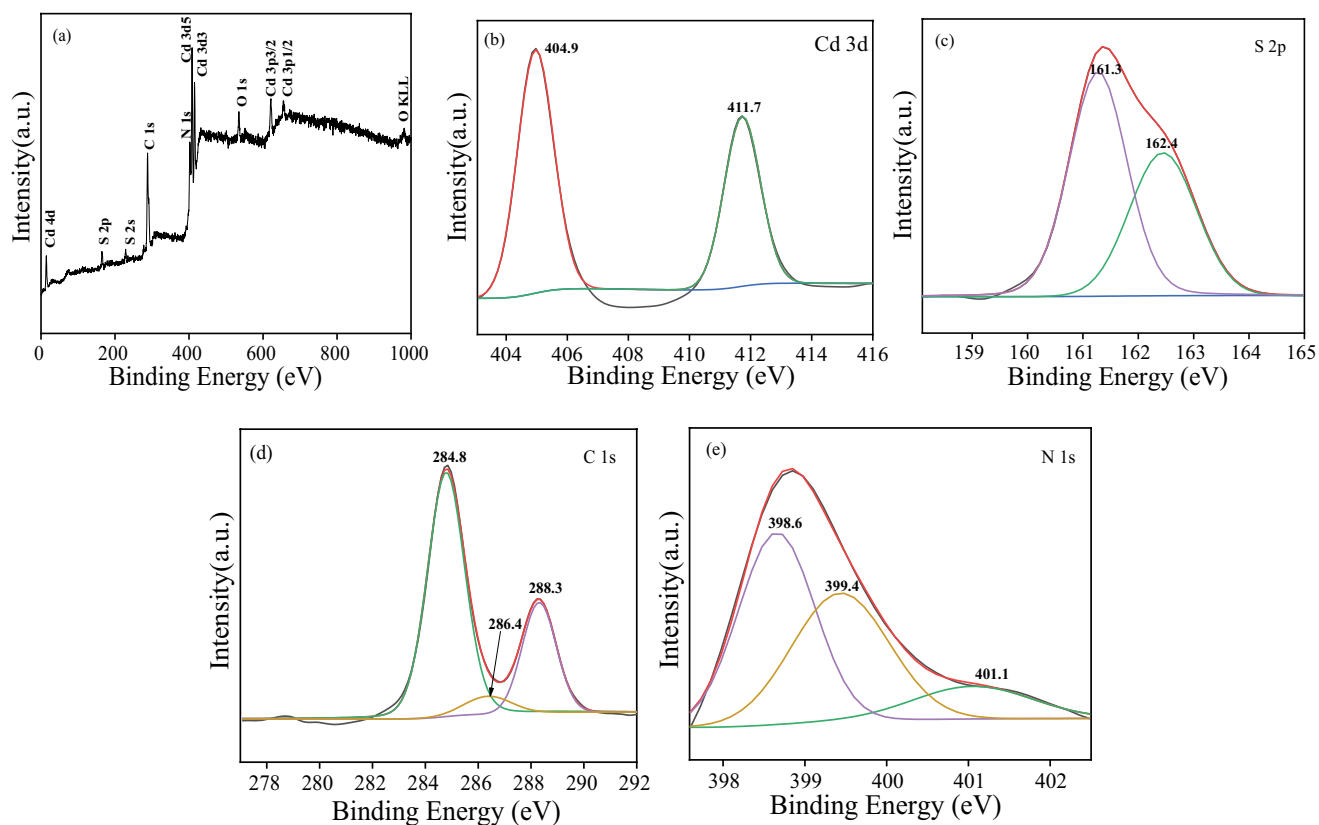


Fig. 4. XPS spectrogram of CNCS-2: (a) survey spectrum, (b) Cd 3d, (c) S 2p, (d) C 1s, and (e) N 1s.

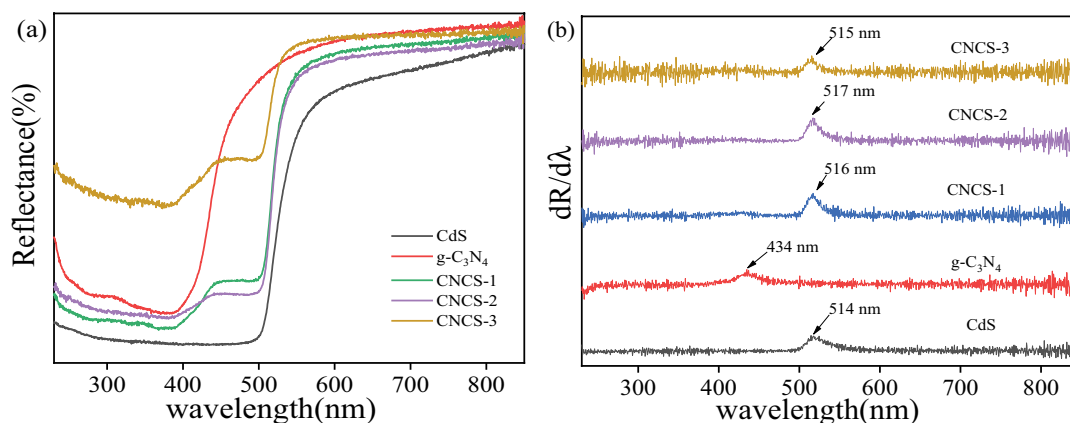


Fig. 5. UV-Vis DRS and (b) the corresponding derivative curves of CdS, $g\text{-C}_3\text{N}_4$, and $g\text{-C}_3\text{N}_4/\text{CdS}$ samples.

the shortest carrier life and higher photogenic carriers recombination, which may be related to the emission of structural defects [35]. However, the PL intensity of $g\text{-C}_3\text{N}_4/\text{CdS}$ nanocomposites is obviously reduced compared with that of pure $g\text{-C}_3\text{N}_4$ and the emission peak of CNCS-2 is the weakest. This indicates that $g\text{-C}_3\text{N}_4/\text{CdS}$ nanocomposites can effectively decrease the recombination of photo-generated electron-hole pairs. The PL spectra of the samples are in good agreement with the results of photocurrent response and EIS measurements.

3.3. Photoelectrochemical analysis

Photoelectrochemical catalytic properties were characterized under simulated sunlight to study photogenic carriers' separation and migration ability for $g\text{-C}_3\text{N}_4/\text{CdS}$ nanocomposites. Fig. 7a shows the transient photocurrent responses and the local magnification of pure CdS, pure $g\text{-C}_3\text{N}_4$, and $g\text{-C}_3\text{N}_4/\text{CdS}$ samples for five on/off cycles under a potential of 0 V. It can be discovered that the photocurrent density for CdS, $g\text{-C}_3\text{N}_4$, CNCS-1, CNCS-2, CNCS-3

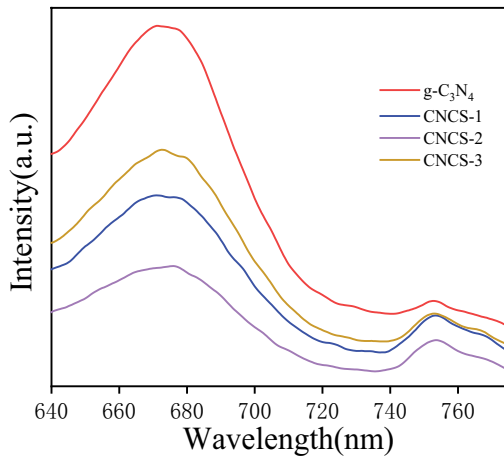


Fig. 6. PL patterns of pure $g\text{-C}_3\text{N}_4$ and $g\text{-C}_3\text{N}_4@CdS$ samples.

are 0.0004, 0.003, 0.008, 0.217, and 0.005 mA cm^{-2} , respectively, while the photocurrent response decreased to zero for all the samples in the dark. The photocurrent rises and falls rapidly with the switching of the light, indicating that the samples possess a fast light response. The photocurrent density of CNCS-2 composites is significantly enhanced and compared with that of pure CdS and $g\text{-C}_3\text{N}_4$ samples. Furthermore, it is worth noting that the value of CNCS-2 samples is maximal, which is approximately 542 times as much as pure CdS and about 72 times larger than that of pure $g\text{-C}_3\text{N}_4$, indicating that the composites exhibit a higher electron-hole pairs separation, and the charge carriers have long lifetimes. This may be due to the intense visible-light absorption of $g\text{-C}_3\text{N}_4@CdS$ heterojunctions. This result is consistent with the interpretation of the PL spectra.

To further study the charge transfer characteristics of the samples, EIS Nyquist plots of pure CdS, pure $g\text{-C}_3\text{N}_4$, and CNCS-2 samples were conducted; as shown in Fig. 7b, the Nyquist plots of the samples exhibit an approximate semicircle-like shape. The semicircle diameter of the Nyquist plots indicates the interfacial carriers

transfer resistance between the electrolyte and electrode [36,37]. The diameter of the arc for CNCS-2 heterojunction is smaller than that of pure CdS and $g\text{-C}_3\text{N}_4$, indicating that the nanocomposites possess lower charge transfer resistance due to the faster interface charge transfer at the CNCS-2 electrolyte interface. Therefore, the catalysts can significantly improve the transfer efficiency of photo-generated carriers, which is beneficial to improve their photoelectrochemical performance.

The Mott-Schottky measurement of pure CdS, pure $g\text{-C}_3\text{N}_4$, and CNCS-2 samples was carried out to estimate the carrier density, the conduction band, and valence band position of a photocatalyst. According to Mott-Schottky formula [38]:

$$\frac{1}{C^2} = \left(\frac{2}{e\epsilon_r\epsilon_0 N_d A} \right) \left(V - V_{FB} - \frac{kT}{e} \right) \quad (1)$$

where V is the applied potential, V_{FB} is the flat band potential, e is the electron charge, ϵ_r is the relative dielectric constant, ϵ_0 is the vacuum dielectric constant, N_d is the majority carrier density, A is the electrode surface area, k is the Boltzmann constant, T is the absolute temperature, and C is the space charge capacitance. At room temperature, kT/e is too small to be ignored, the variation of $1/C^2$ to V of Mott-Schottky plots at different frequencies for pure CdS, pure $g\text{-C}_3\text{N}_4$, and CNCS-2 sample as shown in Fig. 8. It can be seen from Fig. 8a–c that all samples display n -type semiconductor properties because of the positive slope in the linear region of the Mott-Schottky plots. The flat band potential (V_{FB}) obtained from the Mott-Schottky plot by extrapolating the linear portion to the V -axis, the V_{FB} values for pure CdS, pure $g\text{-C}_3\text{N}_4$, and CNCS-2 samples are -0.52 , -1.03 , and -1.48 eV vs SCE, respectively. For n -type semiconductors, the CB edge potential is approximately equal to the flat band potential [38]. According to UV-vis absorption spectrum analysis, $E_g = 2.41$ eV for pure CdS and 2.86 eV for $g\text{-C}_3\text{N}_4$, the corresponding VB potential is estimated to be 1.90 and 1.82 eV by $E_{VB} = E_g + E_{CB}$.

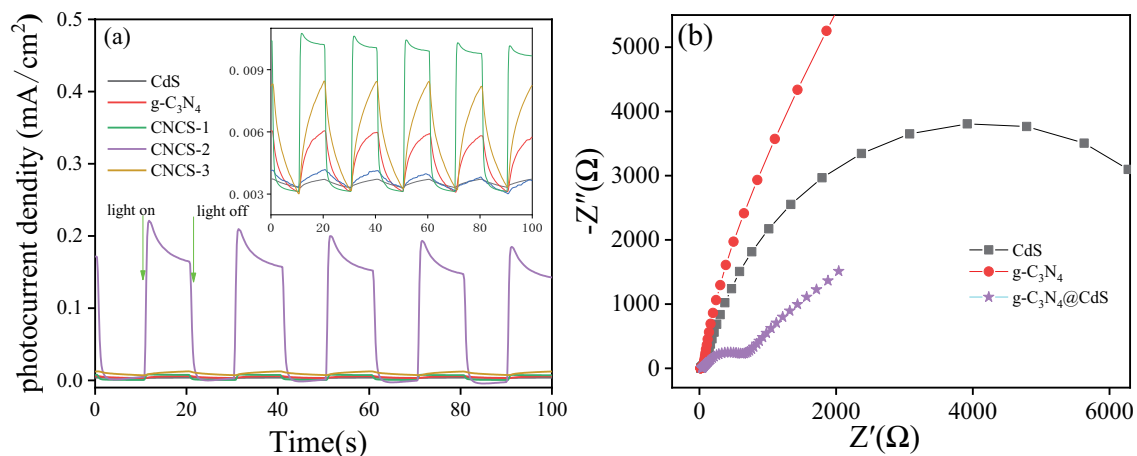


Fig. 7. (a) Transient photocurrent responses of pure CdS, pure $g\text{-C}_3\text{N}_4$, and $g\text{-C}_3\text{N}_4@CdS$ samples, (b) EIS Nyquist plots of pure CdS, pure $g\text{-C}_3\text{N}_4$ and CNCS-2.

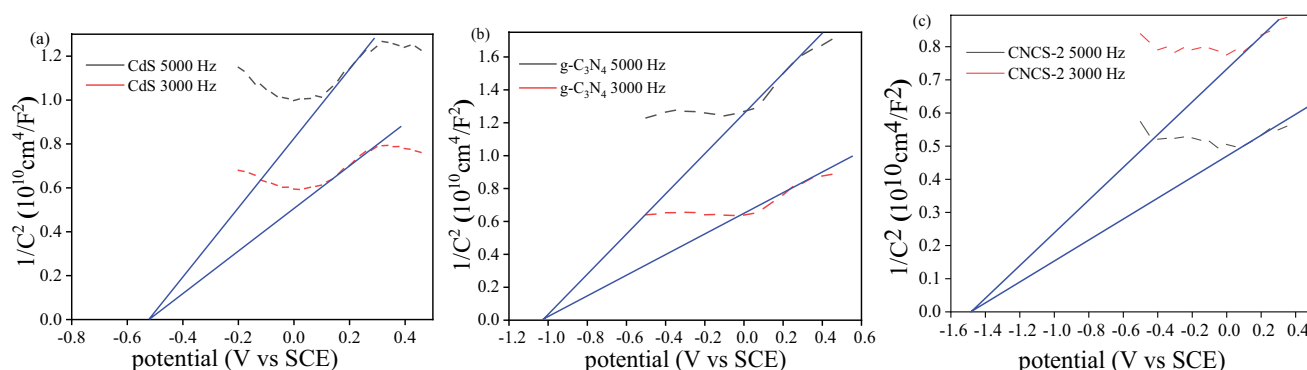


Fig. 8. Mott-Schottky plots for (a) pure CdS, (b) pure $g\text{-C}_3\text{N}_4$ and (c) CNCS-2.

3.4. Photocatalytic activity

Fig. 9a shows the photocatalytic activities of pure CdS, pure $g\text{-C}_3\text{N}_4$, and $g\text{-C}_3\text{N}_4@\text{CdS}$ photocatalysts as a function of irradiation time with the degradation of MO under simulated solar irradiation. In blank experiments without photocatalyst, the self-degradation of MO can be ignored, indicating that MO has good stability. After irradiation for 120 min, the degradation rates of pure CdS and $g\text{-C}_3\text{N}_4$ are 22% and 28.4%, respectively. The photocatalytic degradation activity of $g\text{-C}_3\text{N}_4@\text{CdS}$ composites, on the other hand, is significantly enhanced; further, the CNCS-2 composite displays the highest photocatalytic activity, and the degradation rate is about 74.3% after 120 min of illumination.

Fig. 9b displays $\ln(C_t/C_0)$ plots vs irradiation time of the photocatalytic degradation MO. The kinetic characteristics for all samples follow the pseudo-first-order kinetic equation [39]: $\ln(C_t/C_0) = -k_{\text{app}}t$, the reaction rate constants k_{app} of pure CdS, pure $g\text{-C}_3\text{N}_4$, CNCS-1, CNCS-2, CNCS-3 are 0.00166, 0.0023, 0.00609, 0.01116, and 0.00311 min^{-1} , respectively. The rate constant of $g\text{-C}_3\text{N}_4@\text{CdS}$ composites is greater than that of pure CdS and $g\text{-C}_3\text{N}_4$, and CNCS-2 displays the highest rate constant, which is 6.72 times that of pure CdS. The relatively high degradation efficiency of $g\text{-C}_3\text{N}_4@\text{CdS}$ composites is due to effective separation of electron-hole pairs and better r visible-light capture capability, ascribed to the electron transfer between CdS and $g\text{-C}_3\text{N}_4$. The photocatalytic activities measurements are consistent with the result of PL spectra, transient photocurrent response, and EIS tests.

In order to study the main role of active species in the photocatalytic degradation of dyes, isopropanol (IPA), ethanol (EA), and benzoquinone (BQ) were added as free radical capture experiments for scavenging hydroxyl radical ($\cdot\text{OH}$), holes (h^+), and superoxide radical ($\cdot\text{O}_2^-$), respectively [40,41]. As shown in Fig. 9c, after adding EA, IPA, and BQ as scavenging agents, the degradation rate of MO for CNCS-2 decreased from 74.3% to 66.9%, 40%, and 21.2%, respectively. This reveals that $\cdot\text{O}_2^-$ and $\cdot\text{OH}$ are the dominant reaction species in the photocatalytic system.

In Fig. 9a, in blank experiments without photocatalyst, the self-degradation of MO can be ignored, indicating that MO has good stability but the MO concentration decreased

obviously after the addition of photocatalyst; there is charge transfer between MO excited in visible light and semiconductor photocatalyst. Fig. 9c, which reveals $\cdot\text{O}_2^-$ and $\cdot\text{OH}$ are the dominant reaction species in the photocatalytic system, indicates that the catalyst can photosensitize dyes and broaden the range of light responses.

Fig. 9d shows the reusability and durability of CNCS-2 photocatalysts for photocatalytic degradation of MO was investigated for five successive cycles under the same conditions. It is clear that in the fifth cycle, the degradation rate decreases slightly and maintains 65.4% after 600 min of reaction. Therefore, $g\text{-C}_3\text{N}_4@\text{CdS}$ photojunctions photocatalyst possess good catalytic stability and broad application prospects in wastewater treatment. This result also proves that CNCS-2 has good photostability.

3.5. Photocatalytic mechanism

Since the separation, transfer, migration of photo-generated carriers, and the band position of semiconductors determine the photoelectricity catalytic activity, the possible photocatalytic mechanism of $g\text{-C}_3\text{N}_4@\text{CdS}$ composites under simulated visible-light irradiation is illustrated in Fig. 10. Based on the UV-vis absorption spectrum and Mott-Schottky measurement, the E_g , CB, and VB of pure CdS are 2.42, -0.52, and +1.88 eV, and the E_g , CB, and VB of pure $g\text{-C}_3\text{N}_4$ are 2.85, -1.03, and +1.82 eV, respectively. For $g\text{-C}_3\text{N}_4@\text{CdS}$ heterojunctions, the photo-generated electrons are simultaneously excited from the VB to the CB of pure $g\text{-C}_3\text{N}_4$ and CdS semiconductors under the simulated visible-light irradiation while the holes are left in the valence band of $g\text{-C}_3\text{N}_4$ and CdS, respectively. Since the conduction band potential of CdS is higher than that of $g\text{-C}_3\text{N}_4$, the photoelectrons produced in CdS will spontaneously transfer to the conduction band of $g\text{-C}_3\text{N}_4$ [42]. Moreover, the E_{VB} of $g\text{-C}_3\text{N}_4$ is more positive than that of CdS; the holes of the $g\text{-C}_3\text{N}_4$ valence band can rapidly transfer to the valence band of CdS [36,37]. Since the conduction band potential of CdS is higher than that of $g\text{-C}_3\text{N}_4$, the photoexcited electrons in the CB of $g\text{-C}_3\text{N}_4$ will spontaneously transfer to the CB of CdS, while the photoexcited holes in the VB of CdS can directly move to the VB of $g\text{-C}_3\text{N}_4$ due to the E_{VB} of $g\text{-C}_3\text{N}_4$ is more positive than that of CdS. The photo-generated electron-hole pairs play a vital role in the redox

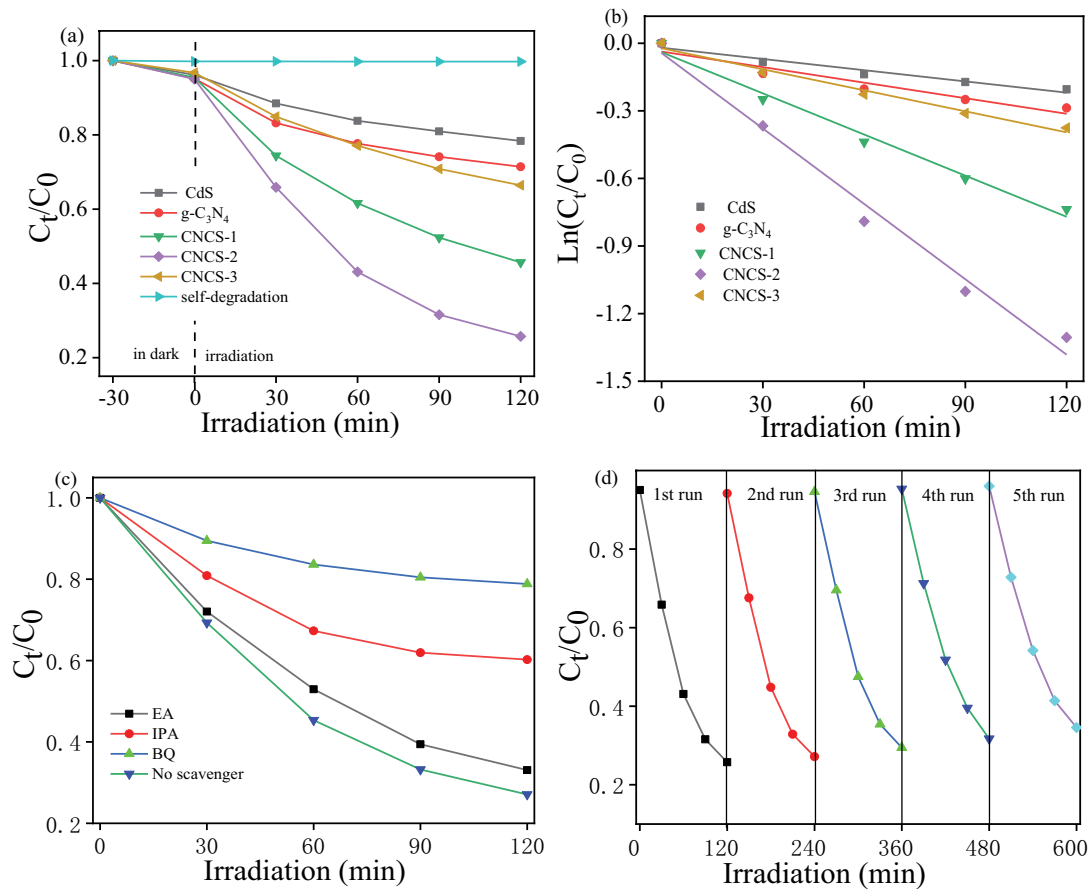


Fig. 9. (a) The photocatalytic degradation of MO over time, (b) polts of $(\ln(C_t/C_0))$ vs. irradiation time for pure CdS, $g-C_3N_4$, and $g-C_3N_4@CdS$ samples, (c) the radical species capture experiment, and (d) recyclability of CNCS-2.

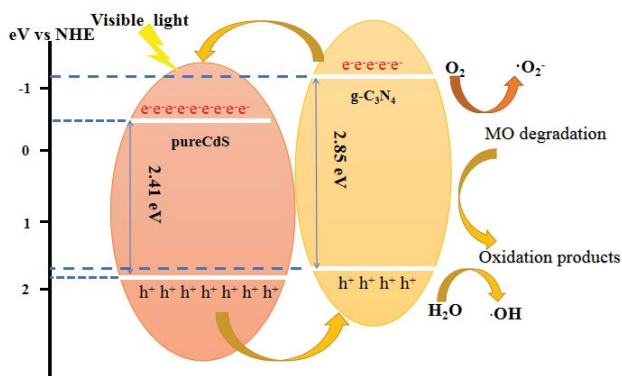


Fig. 10. The schematic diagram of photocatalytic mechanism of the $g-C_3N_4@CdS$ composites under simulated sunlight.

coupling process. Photo-generated electron-hole pairs are effectively separated and the light absorption range is expanded, which can significantly improve the photoelectric catalytic performance of $g-C_3N_4@CdS$ heterojunctions. The photo-generated electrons react with O_2 in the water to form superoxide radicals ($\cdot O_2^-$) and the holes react with water to form hydroxyl radicals ($\cdot OH$), which participate in the degradation of MO dye molecules.

4. Conclusions

A high-efficiency $g-C_3N_4@CdS$ photojunctions photocatalyst driven by visible light was successfully prepared. $g-C_3N_4@CdS$ nanocomposites are hexagonal structures, CdS nanorod structures are partially wrapped by $g-C_3N_4$. $g-C_3N_4@CdS$ composites exhibit good visible-range absorption features and CNCS-2 exhibits the smallest band gap. Heterojunctions accelerate the separation and migration of photo-generated electron-hole pairs and inhibit the recombination of photo-generated carriers, which can show from the PL spectra, transient photocurrent response, and EIS measurements of $g-C_3N_4@CdS$ composites. $g-C_3N_4@CdS$ heterojunctions photocatalysts exhibit enhanced photocatalytic activity and excellent recyclability property to degrade MO than the pure photocatalysts under visible-light illumination. $\cdot O_2^-$ and $\cdot OH$ play a crucial role in the photocatalytic degradation of MO.

Acknowledgements

This work was supported by the National Natural Science Foundation of China (51261015), Natural Science Foundation of Gansu Province, China (1308RJZA238), and Hong Liu First-Class Disciplines Development Program of Lanzhou University of Technology.

References

- [1] F. Chen, X.F. Zou, C. Chen, Q. Hu, Y.Q. Wei, Y.Z. Wang, B. Xiang, J.L. Zhang, Surfactant-free synthesis of homogeneous nano-grade cadmium sulfide grafted reduced graphene oxide composite as a high-activity photocatalyst in visible light, *Ceram. Int.*, 45 (2019) 14376–14383.
- [2] T.L. Feng, S.Y. Tao, D. Yue, Q.S. Zeng, W.H. Chen, B. Yang, Recent advances in energy conversion applications of Carbon Dots: from optoelectronic devices to electrocatalysis, *Small*, 16 (2020) 1–30.
- [3] L. Ma, Z.Q. Wei, X.L. Zhu, J.H. Liang, X.D. Zhang, Synthesis and photocatalytic properties of Co-doped $Zn_{1-x}Co_xMn_2O$ hollow nanospheres, *J. Nanomater.*, 2019 (2019) 1–9.
- [4] Z.Z. Liang, R.C. Shen, Y.H. Ng, P. Zhang, Q.J. Xiang, X. Li, A review on 2D MoS_2 cocatalysts in photocatalytic H₂ production, *J. Mater. Sci. Technol.*, 56 (2020) 89–121.
- [5] S.H. Aswathy, C.C. Mohan, P.S. Unnikrishnan, A.G. Krishnan, M.B. Nair, Decellularization and oxidation process of bamboo stem enhance biodegradation and osteogenic differentiation, *Mat. Sci. Eng. C-Mater.*, 119 (2021) 111500–111500.
- [6] I. Khan, N. Zada, I. Khan, M. Sadiq, K. Saeed, Enhancement of photocatalytic potential and recoverability of Fe_3O_4 nanoparticles by decorating over monoclinic zirconia, *J. Environ. Health. Sci.*, 18 (2020) 1473–1489.
- [7] S.E. Philo, E.K. Keim, R. Swanson, A.Q.W. Ong, E.A. Burnor, A.L. Kossik, J.C. Harrison, B.A. Demeke, N.A. Zhou, N.K. Beck, J.H. Shirai, J.S. Meschke, A comparison of SARS-CoV-2 wastewater concentration methods for environmental surveillance, *Sci. Total. Environ.*, 760 (2020) 144215–144215.
- [8] J.J. Rueda-Marquez, I. Levchuk, P.F. Ibanez, M. Sillanpaa, A critical review on application of photocatalysis for toxicity reduction of real wastewaters, *J. Cleaner Prod.*, 258 (2020) 1–13.
- [9] L. Cai, J. Hu, M. Li, P. Yin, Hybrid catalysts of molybdovanadophosphoric acid and $g-C_3N_4$ with tunable bandgaps, *Dalton Trans.*, 49 (2020) 10724–10728.
- [10] W.L. Oliveira, M.A. Ferreira, H.A.J.L. Mourao, M.J.M. Pires, V. Ferreira, H.F. Gorgulho, D.F. Cipriano, J.C.C. Freitas, V.R. Mastelaro, O.R. Nascimento, D.E.C. Ferreira, F. Ramos Fioravante, M.C. Pereira, J.P. de Mesquita, Heterogeneous Fenton-like surface properties of oxygenated graphitic carbon nitride, *J. Colloid Interface Sci.*, 587 (2020) 479–488.
- [11] H. Azizi-Toupkanloo, M. Karimi-Nazarabad, M. Shakeri, M. Eftekhari, Photocatalytic mineralization of hard-degradable morphine by visible light-driven $Ag@g-C_3N_4$ nanostructures, *Environ. Sci. Pollut. Res.*, 26 (2019) 30941–30953.
- [12] Y. Li, S. Zhu, X. Kong, Y. Liang, Z. Li, S. Wu, C. Chang, S. Luo, Z. Cui, In situ synthesis of a novel $Mn_3O_4/g-C_3N_4$ p-n heterostructure photocatalyst for water splitting, *J. Colloid Interface Sci.*, 586 (2021) 778–784.
- [13] K.L. Li, Y. He, P. Chen, H. Wang, J.P. Sheng, W. Cui, G. Leng, Y.H. Chu, Z.M. Wang, F. Dong, Theoretical design and experimental investigation on highly selective Pd particles decorated C_3N_4 for safe photocatalytic NO purification, *J. Hazard. Mater.*, 392 (2020) 1–8.
- [14] N. Guy, Directional transfer of photocarriers on $CdS/g-C_3N_4$ heterojunction modified with Pd as a cocatalyst for synergistically enhanced photocatalytic hydrogen production, *Appl. Surf. Sci.*, 522 (2020) 1–12.
- [15] Y.P. Hou, G.Y. Yuan, S.F. Wang, Z.B. Yu, S.M. Qin, L.L. Tu, Y.M. Yan, X.X. Chen, H.X. Zhu, Y.K. Tang, Nitrofurazone degradation in the self-biased bio-photoelectrochemical system: $g-C_3N_4/CdS$ photocathode characterization, degradation performance, mechanism and pathways, *J. Hazard. Mater.*, 384 (2020) 1–11.
- [16] G.Q. Li, H.O. Liang, G.R. Xu, C.P. Li, J. Bai, Controllable synthesized heterojunction hollow nanotube of $g-C_3N_4/CdS$: enhance visible light catalytic performance for hydrogen production, *J. Phys. Chem. Solids*, 145 (2020) 1–10.
- [17] S. Vadivel, S. Hariganesh, B. Paul, G. Mamba, P. Puviarasu, Highly active novel $CeTiO_3/g-C_3N_3$ photocatalyst with extended spectral response towards removal of endocrine disruptor 2,4-dichlorophenol in aqueous medium, *Colloids Surf., A*, 592 (2020) 1–11.
- [18] S. Wu, J.J. Guo, Y. Wang, $Bi_2O_3CO_3-Bi_2O_3(OH)NO_3/g-C_3N_4$ heterojunction as a visible-light-driven photocatalyst with enhanced photo-generated charge separation, *J. Alloys Compd.*, 818 (2020) 1–10.
- [19] H.R. Kim, B.G. An, Y.W. Chang, M.J. Kang, J.G. Park, J.C. Pyun, Highly sensitive in situ-synthesized cadmium sulfide (CdS) nanowire photosensor for chemiluminescent immunoassays, *Enzyme Microb. Technol.*, 133 (2020) 1–8.
- [20] S. Manchala, A. Gandamalla, N.R. Vempuluru, S. Muthukonda Venkatakrishnan, V. Shanker, High potential and robust ternary $LaFeO_3/CdS$ /carbon quantum dots nanocomposite for photocatalytic H₂ evolution under sunlight illumination, *J. Colloid Interface Sci.*, 583 (2021) 255–266.
- [21] Y. Tan, Z. Zhang, F. Guo, R. Guo, H. Bai, B. Zhang, X. Li, Q. Yang, X. Liu, Effect of morphology transformation on photocatalytic performance of CdS crystal, *J. Mater. Sci. - Mater. Electron.*, 31 (2020) 20315–20324.
- [22] B. Palanisamy, C.M. Babu, B. Sundaravel, S. Anandan, V. Murugesan, Sol-gel synthesis of mesoporous mixed Fe_2O_3/TiO_2 photocatalyst: application for degradation of 4-chlorophenol, *J. Hazard. Mater.*, 252 (2013) 233–242.
- [23] J.C. Wang, C.X. Cui, Y. Li, L. Liu, Y.P. Zhang, W.N. Shi, Porous Mn doped $g-C_3N_4$ photocatalysts for enhanced synergistic degradation under visible-light illumination, *J. Hazard. Mater.*, 339 (2017) 43–53.
- [24] X. Dai, M.L. Xie, S.G. Meng, X.L. Fu, S.F. Chen, Coupled systems for selective oxidation of aromatic alcohols to aldehydes and reduction of nitrobenzene into aniline using $CdS/g-C_3N_4$ photocatalyst under visible light irradiation, *Appl. Catal., B*, 158 (2014) 382–390.
- [25] K. Cheng, H. Wang, J. Bang, D. West, J. Zhao, S. Zhang, Carrier dynamics and transfer across the CdS/MoS_2 interface upon optical excitation, *J. Phys. Chem. Lett.*, 11 (2020) 6544–6550.
- [26] H.X. Zhao, S. Cui, L. Yang, G.D. Li, N. Li, X.T. Li, Synthesis of hierarchically meso-macroporous TiO_2/CdS heterojunction photocatalysts with excellent visible-light photocatalytic activity, *J. Colloid Interface Sci.*, 512 (2018) 47–54.
- [27] X.L. Xiang, B.C. Zhu, B. Cheng, J.G. Yu, H.J. Lv, Enhanced photocatalytic H₂-Production activity of CdS Quantum Dots using Sn^{2+} as cocatalyst under visible light irradiation, *Small*, 16 (2020) 1–9.
- [28] Z. Wang, Y. Chen, L. Zhang, B. Cheng, J. Yu, J. Fan, Step-scheme CdS/TiO_2 nanocomposite hollow microsphere with enhanced photocatalytic CO₂ reduction activity, *J. Mater. Sci. Technol.*, 56 (2020) 143–150.
- [29] Q. Dong, M.A.M. Sanchez, G.H. Sun, M. Toutounji, S.H. Dong, Tripartite entanglement measures of generalized GHZ state in uniform acceleration, *Chin. Phys. Lett.*, 36 (2019) 1–5.
- [30] X.L. Fan, T. Wang, B. Gao, H. Gong, H.R. Xue, H. Guo, L. Song, W. Xia, X.L. Huang, J.P. He, Preparation of the $TiO_2/Graphitic$ Carbon Nitride core-shell array as a photoanode for efficient photoelectrochemical water splitting, *Langmuir*, 32 (2016) 13322–13332.
- [31] N. Xiao, S.S. Li, S. Liu, B.R. Xu, Y.D. Li, Y.Q. Gao, L. Ge, G.W. Lu, Novel Pt/Pd alloy nanoparticle-decorated $g-C_3N_4$ nanosheets with enhanced photocatalytic activity for H₂ evolution under visible light irradiation, *Chin. J. Catal.*, 40 (2019) 352–361.
- [32] Z. Khan, T.R. Chetia, A.K. Vardhaman, D. Barpuzary, C.V. Sastri, M. Qureshi, Visible light assisted photocatalytic hydrogen generation and organic dye degradation by CdS-metal oxide hybrids in presence of graphene oxide, *RSC Adv.*, 2 (2012) 12122–12128.
- [33] H. Ouyang, H.Q. Huang, H.G. Wang, X.M. Zheng, The morphology evolution of nitrogen-doped carbon quantum dots/hollow TiO_2 composites and their applications in photocatalysis, *J. Mater. Sci.*, 55 (2020) 976–989.
- [34] J. Zheng, L. Zhang, Incorporation of CoO nanoparticles in 3D marigold flower-like hierarchical architecture $MnCo_2O_4$ for highly boosting solar light photo-oxidation and reduction ability, *Appl. Catal., B*, 237 (2018) 1–8.

- [35] D.D. Ren, W.N. Zhang, Y.N. Ding, R.C. Shen, Z.M. Jiang, X.Y. Lu, X. Li, In situ fabrication of robust cocatalyst-free CdS/g-C₃N₄ 2D-2D step-scheme heterojunctions for highly active H₂ evolution, *Sol. RRL.*, 4 (2020) 1–11.
- [36] C. Guo, K. Tian, L. Wang, F. Liang, F. Wang, D. Chen, J. Ning, Y. Zhong, Y. Hu, Approach of fermi level and electron-trap level in cadmium sulfide nanorods via molybdenum doping with enhanced carrier separation for boosted photocatalytic hydrogen production, *J. Colloid Interface Sci.*, 583 (2021) 661–671.
- [37] J.Q. Pan, Z.J. Dong, B.B. Wang, Z.Y. Jiang, C. Zhao, J.J. Wang, C.S. Song, Y.Y. Zheng, C.R. Li, The enhancement of photocatalytic hydrogen production via Ti³⁺ self-doping black TiO₂/g-C₃N₄ hollow core-shell nano-heterojunction, *Appl. Catal., B*, 242 (2019) 92–99.
- [38] A.L. Jin, Y.S. Jia, C.F. Chen, X. Liu, J.Z. Jiang, X.S. Chen, F. Zhang, Efficient photocatalytic hydrogen evolution on band structure tuned polytriazine/heptazine based carbon nitride heterojunctions with ordered needle-like morphology achieved by an in situ molten salt method, *J. Phys. Chem. C*, 121 (2017) 21497–21509.
- [39] W.H. Zhao, Z.Q. Wei, L. Zhang, X.J. Wu, X. Wang, Cr doped SnS₂ nanoflowers: preparation, characterization and photocatalytic decolorization, *Mater. Sci. Semicond. Process.*, 88 (2018) 173–180.
- [40] L. Yan, B. Liu, W. Li, T. Zhao, Y. Wang, Q. Zhao, Multiscale cellulose based self-assembly of hierarchical structure for photocatalytic degradation of organic pollutant, *Cellulose*, 27 (2020) 5241–5253.
- [41] R.C. Shen, Y.N. Ding, S.B. Li, P. Zhang, Q.J. Xiang, Y.H. Ng, X. Li, Constructing low-cost Ni₃C/twin-crystal Zn_{0.5}Cd_{0.5}S heterojunction/homojunction nanohybrids for efficient photocatalytic H₂ evolution, *Chin. J. Catal.*, 42 (2021) 25–36.
- [42] D.D. Ren, Z.Z. Liang, Y.H. Ng, P. Zhang, Q.J. Xiang, X. Li, Strongly coupled 2D-2D nanojunctions between P-doped Ni₂S (Ni₂SP) cocatalysts and CdS nanosheets for efficient photocatalytic H₂ evolution, *Chem. Eng. J.*, 390 (2020) 1–9.